AGU PUBLICATIONS

JGR

Journal of Geophysical Research: Atmospheres

RESEARCH ARTICLE
10.1002/2015JD024559

Key Points:
- Enhanced soil moisture drying occurred over transitional regions
- Precipitation dominantly affect soil moisture change at interannual to decadal time scales
- The enhanced soil drying was primarily caused by global warming

Correspondence to:
J. Huang,
hjp@lzu.edu.cn

Citation:
Cheng, S., and J. Huang (2016), Enhanced soil moisture drying in transitional regions under a warming climate, *J. Geophys. Res. Atmos.*, *121*, doi:10.1002/2015JD024559.

Received 24 NOV 2015
Accepted 22 FEB 2016
Accepted article online 26 FEB 2016

Enhanced soil moisture drying in transitional regions under a warming climate

Shanjun Cheng[1] and Jianping Huang[1]

[1]Key Laboratory for Semi-Arid Climate Change of the Ministry of Education, College of Atmosphere Sciences, Lanzhou University, Lanzhou, China

Abstract We analyzed global trends of soil moisture for the period 1948–2010 using the Global Land Data Assimilation System data set. Soil moisture was dominated by negative trends, with pronounced drying over East Asia and the Sahel. Spatial analysis according to climatic region revealed that the most obvious drying occurred over transitional regions between dry and wet climates. The noticeable drying first took place in the humid transitional regions and extended to the dry transitional regions, beginning in the 1980s. The variability of soil moisture was notably related to the changes in precipitation and temperature, but with different roles. For the global average, precipitation had a dominant effect on the variability of soil moisture at interannual to decadal time scales, but temperature was the main cause of the long-term trend of soil moisture on the whole. The enhanced soil drying in the transitional regions was primarily caused by global warming, which is illustrated by regression analysis and the land surface model.

1. Introduction

Soil moisture plays an important role in environmental processes through its influence in controlling mass and energy exchanges between the land surface and atmosphere [*Seneviratne et al*., 2010]. It has a significant impact on evapotranspiration rates, soil thermal parameters, surface albedo, and Bowen ratio and thus has an effect on the planetary boundary layer regime, clouds, and precipitation [*Cook et al*., 2006; *Findell and Eltahir*, 2003a, 2003b; *Guan et al*., 2009]. The variability of soil moisture, especially soil moisture drying, has an important relationship with heat waves [*Hirschi et al*., 2011; *Lorenz et al*., 2012], dust outbreaks [*Kim and Choi*, 2015], and plant productivity and survival [*Ciais et al*., 2005; *Reichstein et al*., 2007; *Huang et al*., 2015b]. Therefore, studying soil moisture and its variability is crucial to understanding climate change and land-atmosphere interactions.

Traditionally, changes in soil moisture and its relationship with the climate system have been studied via ground-based measurements [*Brocca et al*., 2011; *Guan et al*., 2009; *Huang et al*., 2008; *Wang et al*., 2010]. However, as in situ observations are commonly scarce and limited in time and space, most observational studies have been performed over short temporal and small regional scales. Estimates of large-scale and long-term variability of soil moisture are mainly based on the outputs of remote sensing [*Dorigo et al*., 2012], model simulations [*Yang et al*., 2011], data assimilations [*Yang et al*., 2007, 2009], or various substitute drought indices, such as the Palmer Drought Severity Index (PDSI) [*Dai et al*., 2004], standardized precipitation index [*Wang et al*., 2015], and so on. Both remote sensing and model simulations have revealed an overall drying trend with apparent regional variation in soil moisture trends [*Dorigo et al*., 2012; *Sheffield and Wood*, 2008]. Despite the use of different types of data sets, some common features of soil moisture change have been captured, especially the drying across East Asia and the Sahel. These regions are mainly transitional climate regions between dry and wet climates, which may be the areas most sensitive to global changes because of their fragile ecosystems [*Huang et al*., 2015a, 2015b]. In these regions, potential evaporation exceeds precipitation, and landscapes are characterized by dry climates, low vegetation cover, low nutrition content, and low capacity for water conservation in the soil.

In this paper, we investigate soil moisture trends and report on the relationships between soil moisture trends and climate regions. We also investigate the forcing mechanisms behind precipitation and temperature affecting soil moisture variability and soil drying by means of regression analysis and model simulation. The trend analysis of soil moisture is based on a simulation output from the National Centers for Environmental Prediction/Oregon State University/Air Force/Hydrologic Research Lab (Noah) land surface model [*Chen and Dudhia*, 2001; *Chen et al*., 1996, 1997] derived from the Global Land Data Assimilation System (GLDAS). The model used for mechanism analysis is the community Noah land surface model with

multiparameterization options (Noah-MP) augmented from the Noah land surface model [*Niu et al.*, 2011; *Yang et al.*, 2011]. This is important for deepening our understanding of regional drying and taking reasonable measures to improve the ecological environment and actively address climate change.

The paper is organized as follows: The data and methods are described in section 2. In section 3, we present the results of our analysis. In section 4, we present a summary and discussion.

2. Data Sets and Methods

2.1. GLDAS Data

The surface air temperature, precipitation, and soil moisture data used here are the monthly GLDAS version 2 product (GLDAS-2) for the period from January 1948 to December 2010, with a horizontal resolution of $1° \times 1°$ [*Rodell et al.*, 2004]. The precipitation is the sum of rainfall and snowfall, and the soil moisture data are configured with four vertical layers from the surface to the bottom at 200 cm. The depths of the four soil layers range from 0 to 10 cm, 10 to 40 cm, 40 to 100 cm, and 100 to 200 cm, and the unit of soil moisture has been changed to volumetric (m^3/m^3). In view of the comparability of different layers, we use the mean soil moisture from 0 to 200 cm. GLDAS is a global, high-resolution, offline land data assimilation system, developed jointly by the National Aeronautics and Space Administration/Goddard Space Flight Center (NASA/GSFC) and the National Oceanographic and Atmospheric Administration/National Centers for Environmental Prediction (NOAA/NCEP). The goal was to generate optimal fields of land surface states and fluxes by integrating satellite- and ground-based observational data products, using land surface modeling and data assimilation techniques [*Rodell et al.*, 2004]. The GLDAS data set is widely used in data assimilation, validation, weather and climate model initialization, and hydrology [*Lin et al.*, 2008; *Reichle et al.*, 2007]. The GLDAS-2 product is a simulation output from the Noah land surface model [*Chen and Dudhia*, 2001; *Chen et al.*, 1996, 1997], forced with the Princeton meteorological data set [*Sheffield et al.*, 2006].

2.2. Aridity Index

The aridity index (AI), representing the degree of climatic dryness, is defined as the ratio of annual precipitation (P) to annual potential evapotranspiration. Under this quantitative indicator, drylands are defined as regions with an AI of less than 0.65 and are further classified into hyperarid ($AI < 0.05$), arid ($0.05 \le AI < 0.2$), semiarid ($0.2 \le AI < 0.5$), and dry subhumid ($0.5 \le AI < 0.65$) subtypes [*Middleton and Thomas*, 1997]. The hyperarid regions are the driest, followed by arid, semiarid, and dry subhumid regions in all four types of drylands. The AI was provided by *Feng and Fu* [2013] and has been validated. The AI data were calculated from 1948 to 2008, and the spatial resolution of the data is $0.5° \times 0.5°$. In this paper, the resolution of AI data has been interpolated to $1° \times 1°$ using bilinear interpolation to unify with the GLDAS data.

2.3. Methods

We used both regression analysis and multidimensional ensemble empirical mode decomposition (MEEMD) [*Wu et al.*, 2009]. MEEMD is a way to separate spatiotemporally varying trends and spatially nonuniform variability of different time scales based on ensemble empirical mode decomposition (EEMD) [*Huang et al.*, 1998]. In MEEMD, a time series at a grid point is decomposed using EEMD to obtain a set of intrinsic mode functions (IMFs), which are a series of amplitude frequency-modulated oscillatory components. The last IMF, a curve either monotonic or containing only one extremum, can be recognized as the trend of the time series. This trend has low sensitivity to the extension (addition) of new data. This property guarantees that the physical interpretation within specified time intervals does not change with the addition of new data, consistent with a physical constraint that the subsequent evolution of a physical system cannot alter the reality that has already happened. Both EEMD and MEEMD have been widely applied in climate research [*Ji et al.*, 2014; *Wu et al.*, 2011]. In the MEEMD calculation for this paper, the noise added to data has an amplitude of 0.2 standard deviations of the corresponding data and the ensemble number is 400; the number of IMFs is 5.

To study the contributions of different climatic regions to global soil moisture drying, we calculated the contribution rate using the following formula [*Chandler and Scott*, 2011]

$$CR_k = \left(a_k . \sum_{i=1}^{N_k} W_{ki}\right) / \left(A_g . \sum_{i=1}^{N_g} W_i\right)$$

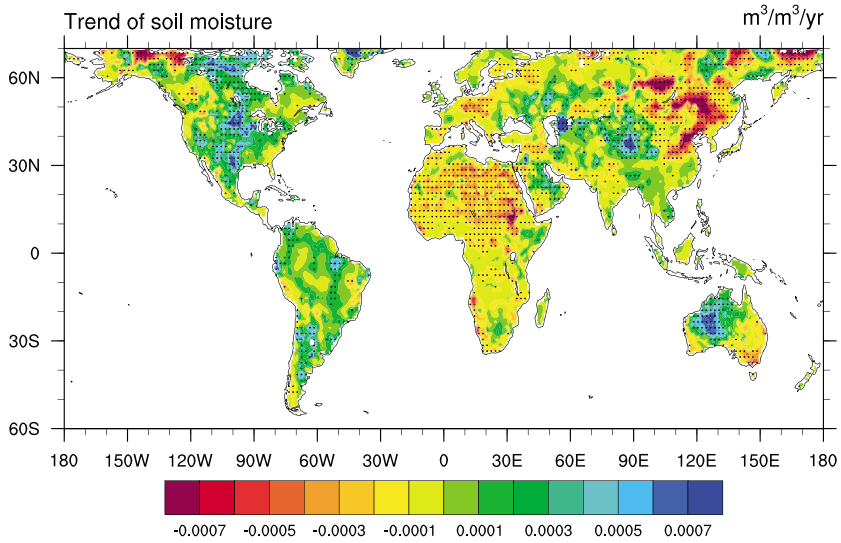

Figure 1. Global annual mean soil moisture trends from 1948 to 2010. The areas marked with crosses denote significant trends at the 95% confidence level according to a two-tailed Student's *t* test.

where a_k is the regional averaged drying trend for region k, A_g is the global averaged drying trend, N_k is the number of drying grids in region k, N_g is the total number of all drying grids over global land, and $W_{ki} = \cos(\theta_i \times \pi/180.0)$, where θ_i is the latitude of the grid i.

2.4. Model and Experimental Design

To study the mechanism of soil moisture variability, especially the contributions of temperature and precipitation change to the soil moisture drying, the Noah-MP was used and three experiments were carried out. The Noah-MP was evaluated by Niu and Yang at local and global scales, who showed the advantages of using multiple optional schemes in modeling simulations [*Niu et al.*, 2011; *Yang et al.*, 2011]. The optional schemes and static data sets are the same as the experiment one in Yang's simulations, which accords with the Noah land surface model [*Yang et al.*, 2011]. We used a 1°×1°, 3-hourly, near-surface meteorological data set processed by GLDAS to drive the model during the period 1948–2010. Because the simulation was initialized arbitrarily, the outputs of the first 2 years were removed to eliminate the influence of initialization. We carried out three experiments: (1) the standard simulation, using the standard meteorological data processed by GLDAS as forcing data; (2) the ConTemp simulation, conducted as departures from the standard simulation but using the composite 3-hourly climatology of near-surface air temperatures over the first 5 years (1948–1952) as the forcing data for all years; and (3) the ConPrep simulation, which is the same as the ConTemp simulation but for a composite climatological precipitation.

3. Results

3.1. Characteristics of Soil Moisture Variability

Figure 1 shows the global distributions of annual mean soil moisture trends from 1948 to 2010. High-latitude areas (above 60°S or 70°N) were ignored, because they were dominated by permafrost (similarly hereinafter). Significant trends ($p = 0.05$) were observed for 40.6% of the global area. Of these, 60.2% were negative and 39.8% were positive. The most prominent drying trends occurred in northern Africa, East Asia, eastern Australia, and southern Europe. Many of the strong drying trends occurred in regions that already had relatively low average soil moisture values. We observed a subtle wetting trend for the central U.S., South America, and western Australia. This might have been induced by precipitation, because precipitation increased significantly over the past several decades in these regions. The soil moisture trend was broadly comparable with various drought indices, such as the PDSI [*Dai*, 2011, 2013; *Wang et al.*, 2014] and the AI [*Feng and Fu*, 2013; *Li et al.*, 2014], which suggests that the broad patterns exhibited by soil moisture data are likely reliable.

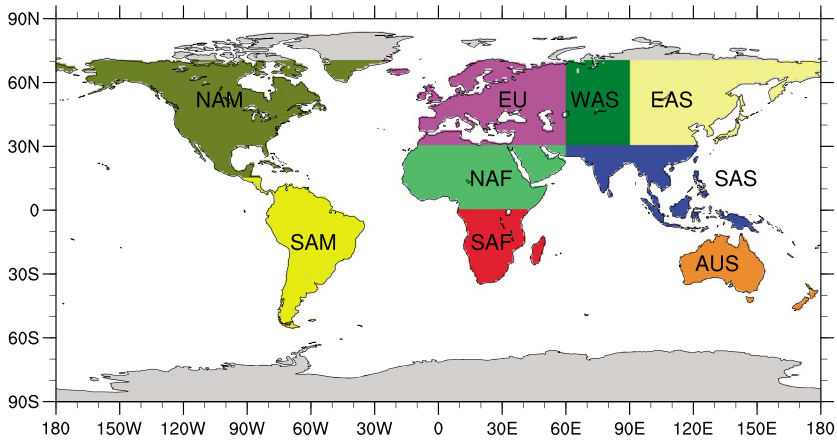

Figure 2. Map of regions used in the analysis. Acronyms are defined in Table 1.

Considering the spatial heterogeneity of soil moisture trends, the continents were divided into nine subregions. The regions (see Figure 2 and Table 1 for details) are classified with reference to Huang's definition [*Huang et al*., 2012, 2015a]. The regional percent acreage and the regional contributions of soil moisture drying to global drying are presented in Table 1. The relative drying acreage can be obtained by comparing the PTA (percentage of total acreage) and PDA (percentage of acreage with soil moisture drying); PDA > PTA means that the region is dominated by soil moisture drying. Of the nine subregions, four exhibited PDA > PTA: Europe (EU), East Asia (EAS), North Africa (NAF), and South Africa (SAF). They were dominated by soil moisture drying at proportions of 63.7%, 78.1%, 84.9%, and 78.9%, respectively. These regions were the most concentrated for soil moisture drying. The other feature of drying, intensity, can be obtained by comparing contributions to global drying and PDA; contributions > PDA means that the drying in the region is very severe. Of the EU, EAS, NAF, and SAF regions, only EAS and NAF exhibited contributions > PDA. The PTA values for EAS and NAF were 12.3% and 16.6%, respectively, but the contributions of soil moisture drying to global drying were 28.3% and 31.8%, respectively. Considering the PTA, PDA, and contributions together, the intensity of drying was low despite drying in a large portion of the EU and SAF regions. The drying in the EAS and NAF regions was the most remarkable.

Since the soil moisture variability depends largely on the climatic region, as shown in Figure 1, the regionally averaged soil moisture trend as a function of the climatological mean AI is presented in Figure 3. The climatological mean AI is the annual mean AI for the period from 1961 to 1990, which represents the climatological state. Two minimal values appeared, one for the hyperarid regions with an AI of less than 0.1 and another for the transitional regions between dry and wet climates with an AI range of 0.4 to 0.8. The marked drying trend in the hyperarid regions with an AI of less than 0.1 was mainly caused by the appreciable drying over

Table 1. PTA (Percentage of Total Acreage, the Ratio Between Acreage of Subregions and Global Acreage, Unit: %), PDA (Percentage of Acreage With Soil Moisture Drying, the Ratio Between Drying Acreage of Subregions and Global Drying Acreage, Unit: %), and Contributions of Soil Moisture Drying to Global Drying for Different Subregions[a]

Regions	Latitude/Longitude	PTA	PDA	Contributions
North America (NAM)	15°N–70°N, 180°W–25°W	16.3	8.7	7.4
South America (SAM)	60°S–15°N, 180°W–25°W	13.9	7.0	3.4
Europe (EU)	30°N–70°N, 25°W–60°E	11.7	13.3	10.2
West Asia (WAS)	30°N–70°N, 60°E–90°E	7.2	6.0	4.4
East Asia (EAS)	30°N–70°N, 90°E–180°E	12.3	17.1	28.3
South Asia (SAS)	12°S–30°N, 60°E–180°E	8.2	7.4	2.7
North Africa (NAF)	0°N–30°N, 25°W–60°E	16.6	25.1	31.8
South Africa (SAF)	60°S–0°N, 25°W–60°E	7.6	10.6	7.2
Australia (AUS)	60°S–12°S, 60°E–180°E	6.1	4.8	4.6

[a]Note that the ranges of subregions may differ from the geographic position, and the names may not be entirely accurate.

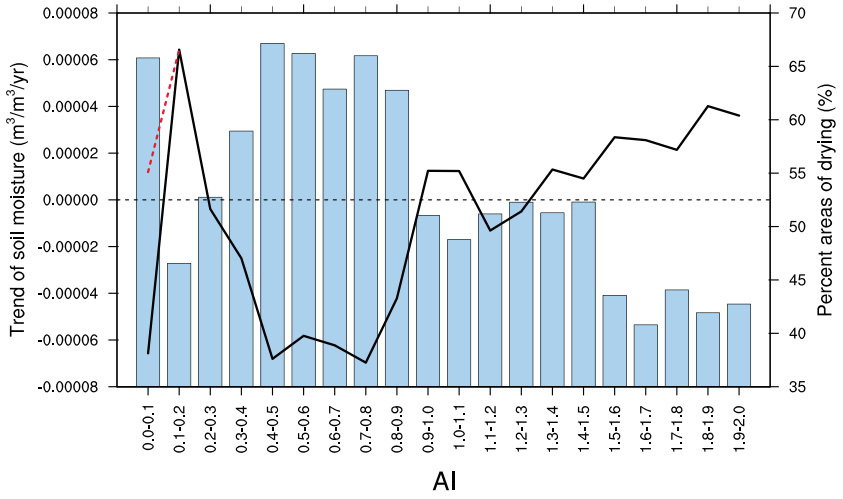

Figure 3. The linear trends of annual mean soil moisture (black line) and percent areas of drying (bars) as a function of the climatological mean AI. The climatological mean AI on the *x* axis is the annual mean AI for the period from 1961 to 1990.

the Sahara, with an AI of less than 0.02. When this region was masked out, the trend changed to 0.00012 $m^3/m^3/10$ yr (shown as the red dashed line in Figure 3), which is negligible. Because the region is relatively small and because it makes little sense to study drying over hyperarid regions, we ignored the marked drying trend over this region. Of particular interest was the soil moisture decrease in transitional regions between dry and wet climates, with a drying peak with an AI range of 0.4 to 0.8. In this paper, we define the regions within the AI range of 0.4 to 0.8 as transitional regions. This greatest variation, which occurred at intermediate moisture contents as illustrated by Figure 2, is consistent with observed soil moisture variation in temperate areas over short temporal and local scales [*Brocca et al*., 2012; *Lawrence and Hornberger*, 2007]. In addition, the percent areas of drying for different climate regions are also presented and show remarkable contributions over the transitional regions. For the transitional regions, more than 60% of areas showed negative soil moisture trends. This indicates that the transitional regions play a dominant role in soil moisture drying, in both area and intensity.

Figure 3 is an intuitional representation of the spatial heterogeneity of soil moisture change; however, the trend over a given time interval cannot accurately reflect how the trend has evolved. To overcome this deficiency, we diagnosed the value increment of the EEMD trend at a given time from the reference time of 1948, that is, $\mathrm{Trend}_{\mathrm{EEMD}}(t) = R_n(t) - R_n(1948)$, representing accumulated drying from 1948 [*Ji et al*., 2014]. $\mathrm{Trend}_{\mathrm{EEMD}}(2010)$ can be recognized as the trend of the soil moisture series from 1948 to 2010, and this trend is markedly consistent with the linear trend shown in Figure 3 (figure omitted). We plotted the evolution of the soil moisture trend as a function of the climatological mean AI (Figure 4) so that the main features of the spatiotemporal evolution of the drying would be more evident. Soil moisture drying was significant only over the transitional regions, but with a two-band structure. The noticeable drying emerged in regions within the AI range of 0.65 to 0.9 (defined as humid transitional regions in this paper) around 1955. The amplitude of the drying grew quickly and reached extremes around the 1990s, with a soil moisture decrease greater than 0.004 m^3/m^3 relative to 1948. Along with the growing amplitude of the drying, the scope of drying expanded toward the drylands, beginning in the 1980s. During the next three decades, the drying in the regions within the AI range of 0.4 to 0.65 (defined as dry transitional regions in this paper), which were the subhumid regions and part of the semiarid regions, became significant. Additionally, the amplitude of the drying was still growing as of 2010, indicating that the soil moisture may continuously decrease during the next few years.

3.2. Mechanism Analysis

Numerous environmental factors (such as soil texture, vegetation, and topography) as well as slight weather disturbances can lead to spatial and temporal variability in soil moisture. Intuitively, changes in precipitation are a key factor affecting the variability of soil moisture, but the latter can also be modified by temperature changes [*Cheng et al*., 2015]. Increased temperatures lead to a higher vapor pressure deficit and evaporative

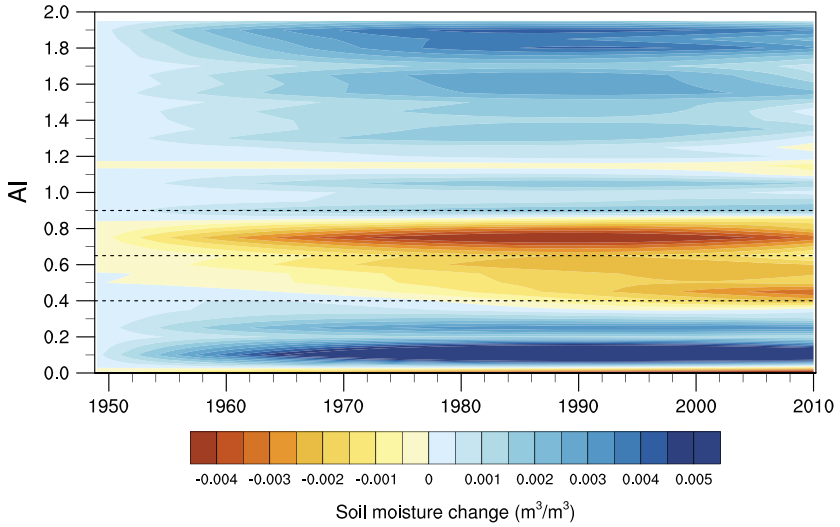

Figure 4. Evolution of the global soil moisture trend as a function of the climatological mean AI. The climatological mean AI on the *y* axis is the annual mean AI for the period from 1961 to 1990.

demand, possibly leading to an increase in evapotranspiration and a decrease in soil moisture. We also calculated the regionally averaged precipitation trend as a function of the climatological mean AI and present it in Figure 5, which shows an enhanced precipitation decrease around the AI range of 0.4 to 0.8. This demonstrates that the precipitation decrease may be a factor causing the enhanced drying over the transitional regions. In addition, the increased temperature also has a great impact on soil drying, as it can lead to larger evapotranspiration and amplify the soil moisture drying caused by decreased precipitation. In the same manner as the precipitation trends, the surface air temperature does not increase everywhere uniformly, which is clearly observable in the dry regions with an AI of less than 0.9. This is because the heat capacity of water is markedly greater than that of soil; the soil heat capacity decreases with decreasing soil moisture. Under these circumstances, the temperature increase of dry land is higher than that of wet land when the change in net radiation is the same. Considering the variability of precipitation and temperature together, only in the transitional regions did both the precipitation decrease and the temperature increase significantly. Thus, the enhanced soil moisture drying in transitional regions may be due to the combined effects of decreased precipitation and increased temperature.

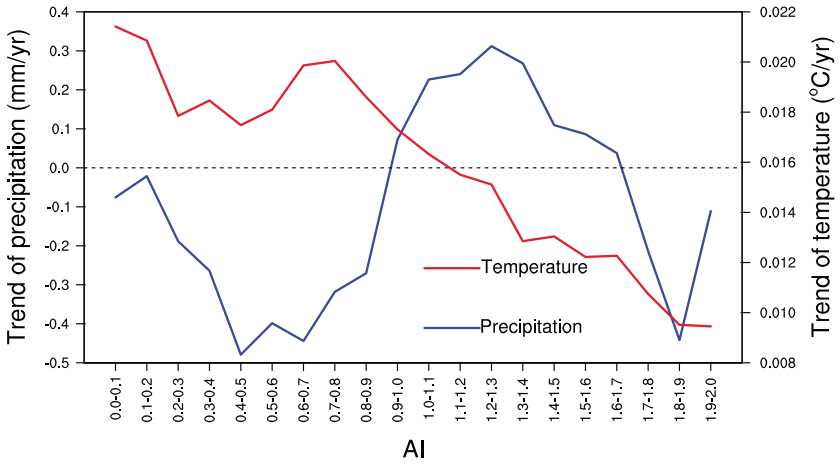

Figure 5. The linear trends of global annual mean temperature and precipitation as a function of the climatological mean AI. The climatological mean AI on the *x* axis is the annual mean AI for the period from 1961 to 1990.

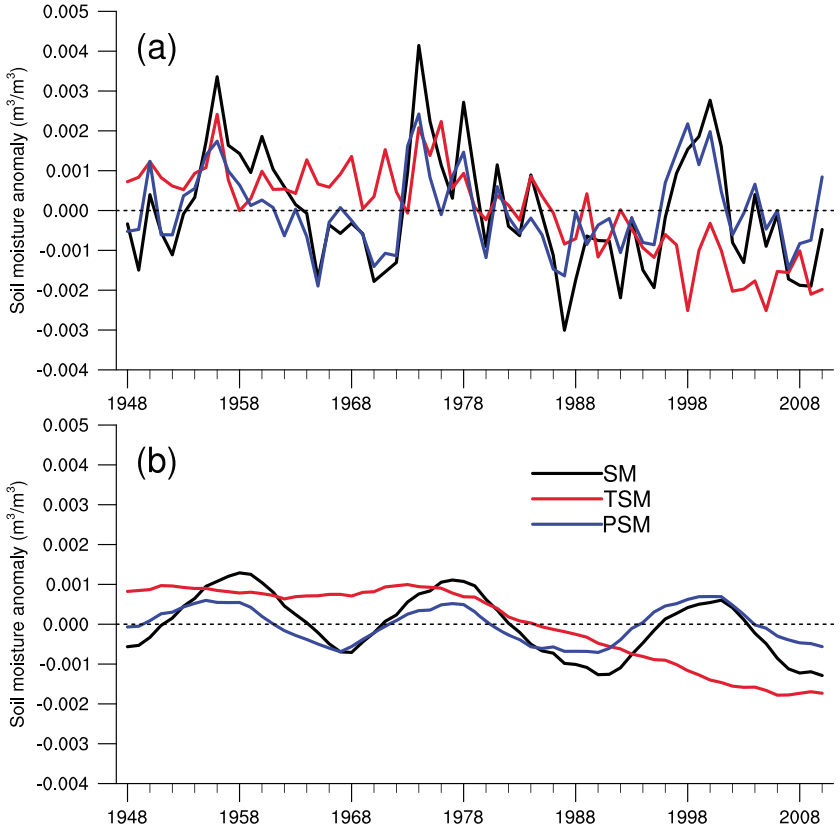

Figure 6. (a) The time series of global annual mean soil moisture (SM), TSM, and PSM anomalies from 1948 to 2010. (b) Also shown are the 7 year running mean time series.

To study the contributions of temperature and precipitation to the soil moisture variability, we applied a simple linear regression to obtain the soil moisture predictand regressed by annual mean precipitation or temperature fields at each grid point. We defined the two predictands by precipitation and temperature as PSM and TSM, respectively. The PSM (TSM) can be roughly determined as the soil moisture component caused by precipitation (temperature). This concept is widely used for separating the external and internal sea surface temperature trends [*Polyakov et al*., 2010; *Ting et al*., 2009]. Figure 6 shows the global annual mean soil moisture, TSM, and PSM anomalies from 1948 to 2010. The time series of the annual mean soil moisture anomaly shows an observable downward trend during the last 63 years with a rate of $-0.000176\ m^3/m^3/10\ yr$, which significantly exceeds the 90% confidence level. Within the long-term linear trends identified, considerable variability occurred at interannual to decadal time scales. The change in soil moisture demonstrates a 20 year cycle period with 10 years of wetting and 10 years of drying from 1948 to 2010, overall. Compared with soil moisture, the long-term variability of the PSM is not significant, despite a decreasing trend over the entire time span, with a rate of $-0.0000284\ m^3/m^3/10\ yr$. However, the time series of PSM correlated strongly ($r = 0.85$) with the soil moisture at interannual to decadal time scales. Unlike the PSM, the time series of TSM shows an inconspicuous decadal variability and observable long-term trend. The rate was $-0.0005\ m^3/m^3/10\ yr$ and significantly exceeds the 99% confidence level. Notably, the TSM changed little before 1976 but decreased significantly since then with a rate of $-0.000869\ m^3/m^3/10\ yr$, which significantly exceeds the 99% confidence level. This significantly decreasing trend coincides with global warming starting from the 1970s. This result suggests that for the global average, precipitation has an effect on the variability of soil moisture at interannual to decadal time scales, but temperature mainly causes the long-term trend of soil moisture on the whole.

On the basis of the soil moisture predictand, the difference between original soil moisture fields and PSM (TSM) can be roughly determined as the soil moisture component without the signal of precipitation

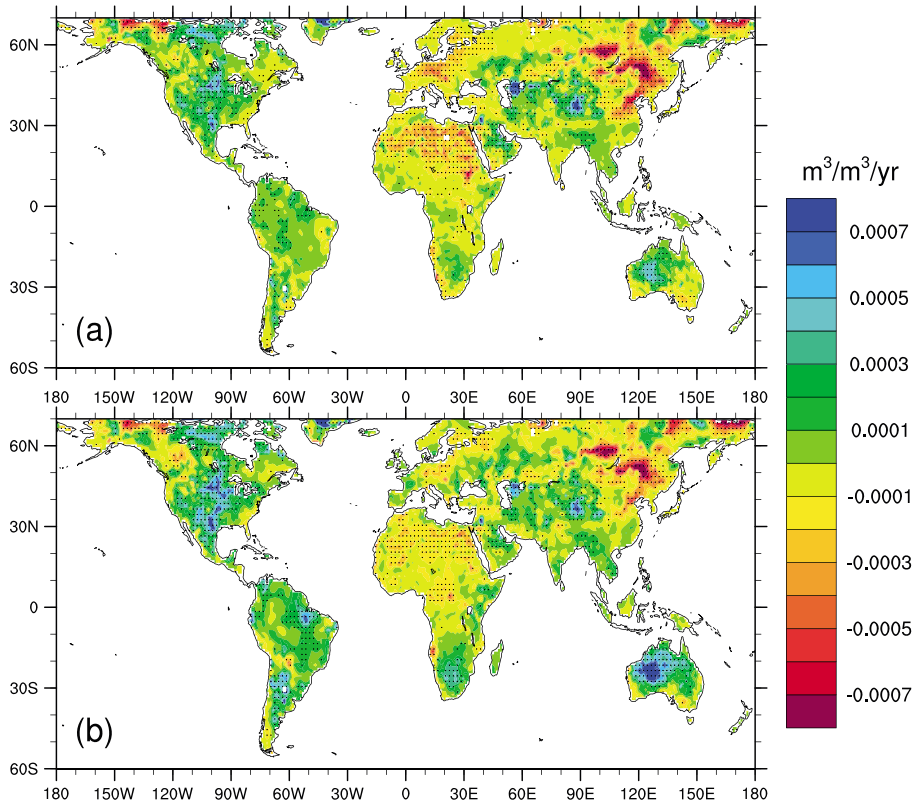

Figure 7. Global trend distributions for annual mean (a) RPSM and (b) RTSM from 1948 to 2010. The areas marked with crosses denote significant trends at the 95% confidence level according to a two-tailed Student's *t* test.

(temperature). We defined the two rest components of soil moisture as RPSM and RTSM, respectively. Figure 7 shows the spatial distributions of the trends of RPSM and RTSM. Comparing Figures 7 and 1, we can see that the pattern of the RPSM and RTSM trends is remarkably similar to the soil moisture trend. However, the magnitudes are small in most areas compared to the soil moisture trend, despite the fact that the trends are also significant at the 95% confidence level over most regions with a significant soil moisture trend. This indicates that both precipitation and temperature have an effect on the long-term soil moisture trend. However, the role of precipitation and temperature in the soil moisture trend is different, as shown in Figures 7a and 7b. Generally speaking, the drying trend of RPSM was more remarkable than that of RTSM. For example, the drying trends over EAS for RPSM and RTSM were −0.00231 and −0.00210 m^3/m^3/10 yr, respectively. In contrast, the wetting trend of RTSM was larger than that of RPSM, especially over western Australia and central North America, where a subtle wetting trend occurred. The wetting trends of RTSM for AUS and NAM were 0.00382 and 0.00231 m^3/m^3/10 yr, respectively, which were larger than those of the RPSM (0.00157 and 0.00163 m^3/m^3/10 yr) and even approximate to the soil moisture trends (0.00280 and 0.00234 m^3/m^3/10 yr). To illustrate the reliability of the results, we demonstrated the significance of difference for soil moisture trend and RPSM (RTSM) trend (figure omitted). Significant difference ($p = 0.05$) for soil moisture trend and RPSM (RTSM) trend was observed for 85% (21%) of the global area. This illustrated that the effect of temperature on the long-term soil moisture trend was significant but precipitation was not. Overall, the precipitation change mainly affects the sign of soil moisture change: decreased precipitation causes drying, and increased precipitation causes wetting. In contrast, global warming has a negative effect on the soil moisture trend over most regions, including the wetting regions, and its effect on soil moisture drying is more apparent than the effect of precipitation.

Similar to Figure 3, the regionally averaged RPSM and RTSM trends as a function of the climatological mean AI are presented in Figure 8. The forms of curves are similar to the soil moisture trend shown in Figure 3, with the driest values in the transitional regions. However, the RPSM trend in the transitional regions is slightly smaller

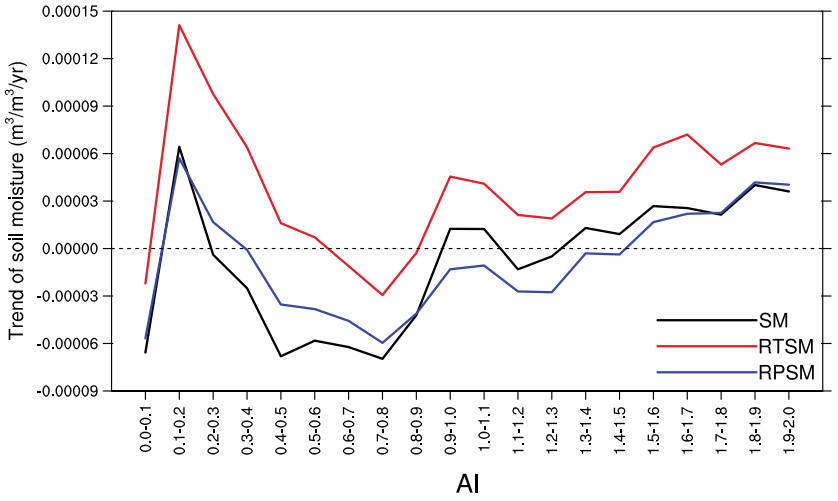

Figure 8. The linear trends of annual mean soil moisture (SM), RTSM, and RPSM as a function of the climatological mean AI. The black line is same as in Figure 3. The climatological mean AI on the *x* axis is the annual mean AI for the period from 1961 to 1990.

than the soil moisture trend. This indicates that precipitation was a factor that caused enhanced soil moisture drying in the transitional regions but that precipitation was not the main controlling factor. When the signal of temperature was removed from the soil moisture, the RTSM trend became positive over most regions. This indicates that temperature was the key factor that caused enhanced soil moisture drying in the transitional regions.

Although we investigated the roles of temperature and precipitation in the soil moisture trend using linear regression methods, the results may have several issues because the climate system is complex and nonlinear. We used the Noah-MP land surface model to verify the results obtained using linear regression methods. To assess the uncertainty of the Noah-MP soil moisture data for each spatial grid, we calculated the temporal correlation coefficient (TCC) and relative root-mean-square difference (RRMSD) between the Noah-MP and GLDAS soil moisture data. The RRMSD was calculated using equation (1):

$$\mathrm{RRMSD} = \mathrm{RMSD}/\mathrm{SM}_{\mathrm{mean}} \times 100\% \quad (1)$$

where RMSD is the root-mean-square difference between the Noah-MP and GLDAS soil moisture data. $\mathrm{SM}_{\mathrm{mean}}$ is the mean soil moisture. We used the TCC to verify the temporal consistency of long-term and interannual variability and the RRMSD to verify the deviations between the data sets. The TCC and RRMSD between GLDAS and Noah-MP soil moisture as a function of the climatological mean AI are presented in Figure 9. Overall, the difference between Noah-MP and GLDAS soil moisture is acceptable. The results show that the correlation coefficient was greater than 0.5 in most regions. In particular, the correlation coefficient for the top three soil layers was greater than 0.7 in most regions and even greater than 0.9 in some regions. The deviation between the data sets was also acceptable, as illustrated by RRMSD, which indicated that the deviations are mainly distributed in the arid regions. The RRMSDs over the humid regions were less than 20% for the four soil layers. In particular, the RRMSDs for the 10–40 cm and 100–200 cm soil layers were less than those of the other two layers. Combining the results of TCC and RRMSD, the difference between Noah-MP and GLDAS soil moisture is acceptable, especially for the 10–40 cm soil layer. Therefore, we chose the 10–40 cm soil moisture here.

We carried out three experiments in this paper (see section 2.3 for details). In the ConPrep (ConTemp) simulation, the precipitation (temperature) was constant during the simulated period, which means the signal of precipitation (temperature) change was removed from the soil moisture. In a certain sense, the ConPrep (ConTemp) simulation is equal to the RPSM (RTSM) field obtained by regression analysis. Similarly, the difference between the standard and ConPrep (ConTemp) simulations (defined as PreSM (TemSM)) is equal to the PSM (TSM) field. Figure 10 presents the global annual mean Noah-MP soil moisture anomaly, TemSM, and PreSM. To be comparable with the Noah-MP soil moisture, the 10–40 cm GLDAS soil moisture is also

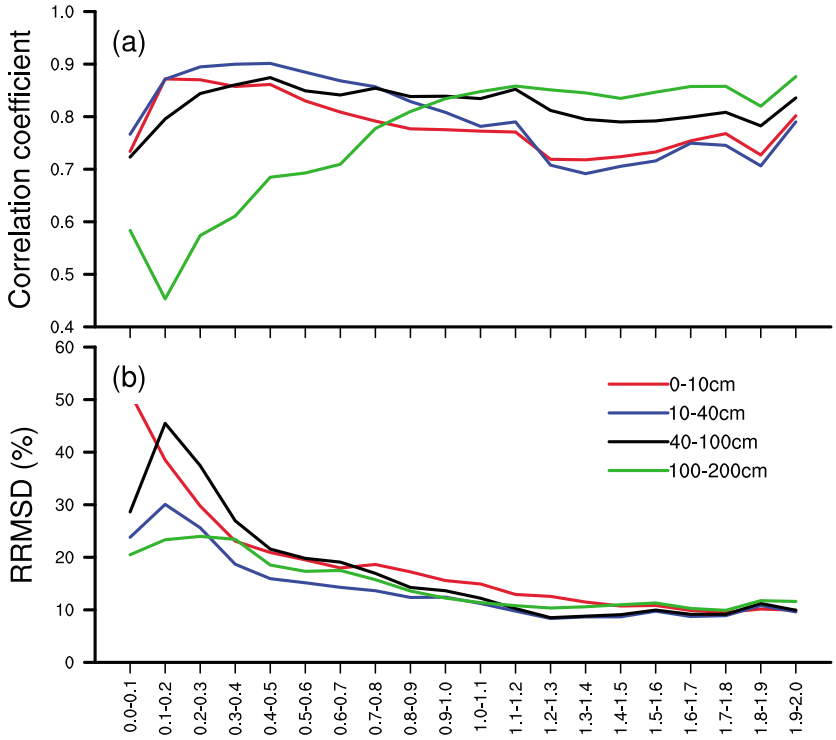

Figure 9. The (a) correlation coefficient and (b) RRMSD between GLDAS and Noah-MP soil moisture as a function of the climatological mean AI. The climatological mean AI on the *x* axis is the annual mean AI for the period from 1961 to 1990.

presented and is coincident with the 0–200 cm GLDAS soil moisture results illustrated in Figure 6. The correlation coefficients between the 0–200 cm and 10–40 cm GLDAS soil moisture are 0.95, 0.99, and 0.99 for soil moisture, TSM, and PSM, respectively, which significantly exceed the 99% confidence level. However, the downward trend of the 10–40 cm soil moisture was more significant than that of the 0–200 cm soil moisture,

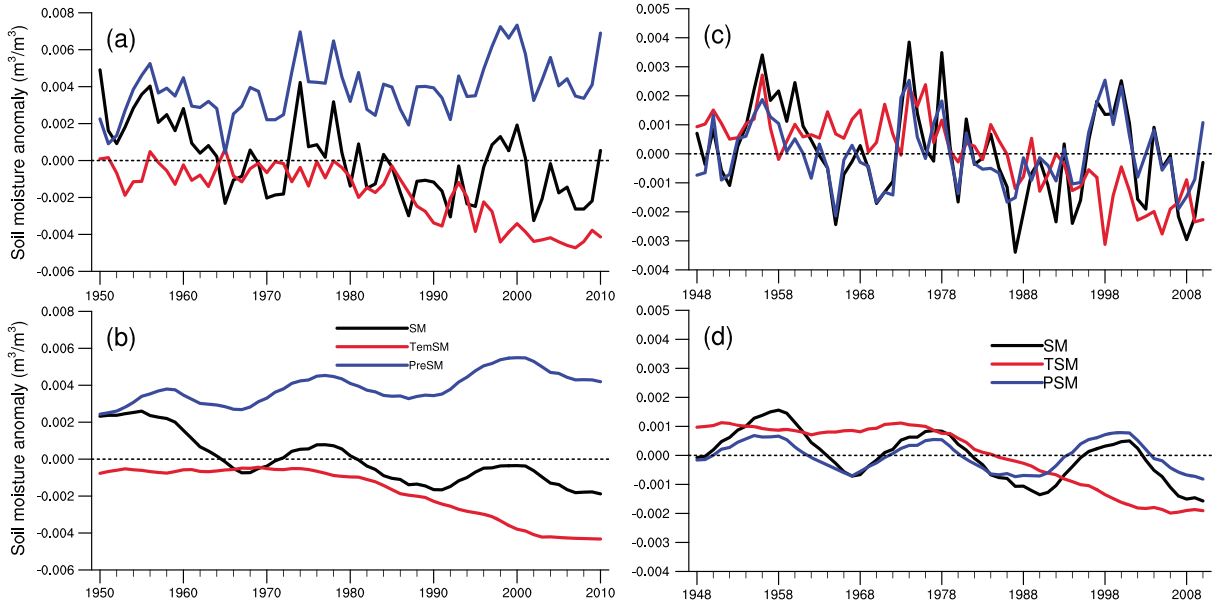

Figure 10. (a) The time series of global annual mean soil moisture (SM) anomaly, TemSM, and PreSM from 1950 to 2010 for Noah-MP soil moisture and (c) the global annual mean soil moisture (SM), TSM, and PSM anomalies from 1948 to 2010 for the 10–40 cm GLDAS soil moisture. (b and d) The 7 year running means for Figures 10a and 10c, respectively.

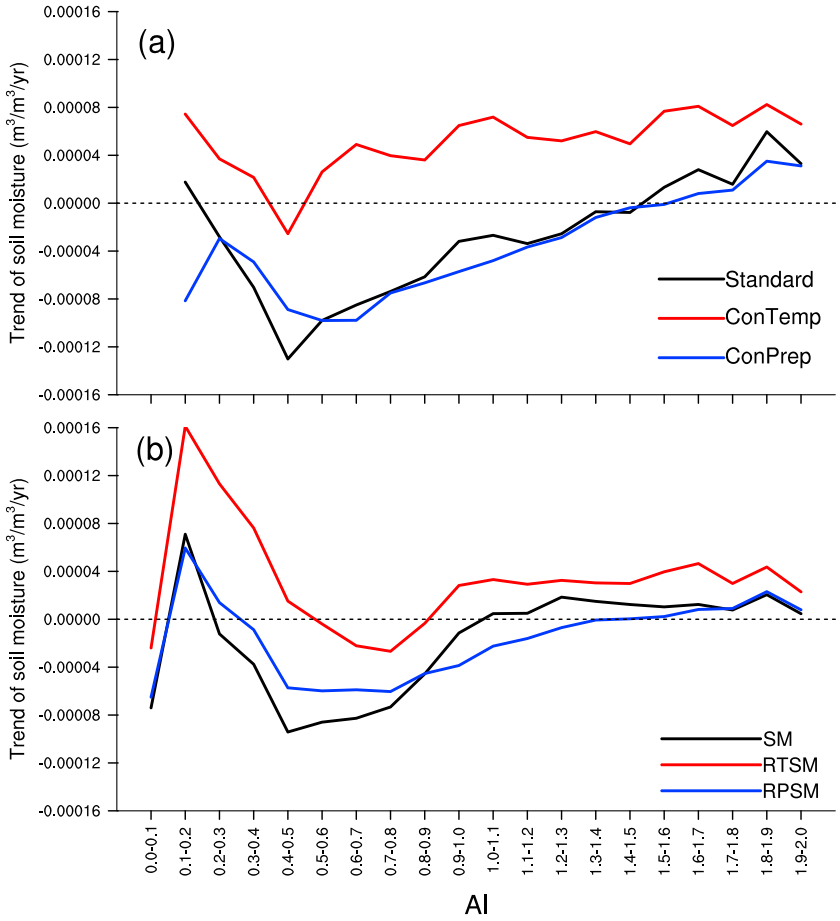

Figure 11. The (a) linear trends of annual mean soil moisture for the three simulations and (b) GLDAS 10–40 cm soil moisture (SM), RTSM, and RPSM as a function of the climatological mean AI. The climatological mean AI on the *x* axis is the annual mean AI for the period from 1961 to 1990. The value for the regions within the AI range of 0 to 0.1 in Figure 11a was unconventionally small, so it was removed.

with a rate of −0.000273 m^3/m^3/10 yr, which significantly exceeds the 95% confidence level. In addition, the time series of the Noah-MP soil moisture anomaly is remarkably similar to the GLDAS soil moisture at interannual to decadal time scales, with a correlation coefficient of 0.88, which significantly exceeds the 99% confidence level. The time series of the annual mean soil moisture anomaly shows an observable downward trend during the last 63 years with a rate of −0.000642 m^3/m^3/10 yr, which significantly exceeds the 99% confidence level. In contrast to the PSM, the PreSM shows an increasing trend over the entire time span, with a rate of 0.00037 m^3/m^3/10 yr. However, the time series of PreSM is strongly correlated ($r = 0.89$) with the Noah-MP simulated soil moisture at interannual to decadal time scales. Similar to the TSM, the time series of TemSM shows an inconspicuous decadal variability and observable long-term trend with three periods: a gentle period before 1980, rapid drying from 1981 to 2001, and a drying hiatus since 2002. This result suggests that precipitation has an effect on the variability of soil moisture at interannual to decadal time scales, but temperature mainly caused the long-term trend of soil moisture, which is in accordance with the results illustrated by the soil moisture predictand.

Additionally, the linear trends of annual mean soil moisture for different experiments as a function of the climatological mean AI are presented in Figure 11. The value for the regions within the AI range of 0 to 0.1 was unconventionally small, so it was removed. To be coincident with the Noah-MP simulated soil moisture, the linear trends of annual mean soil moisture, RTSM, and RPSM for 10–40 cm are also presented and are remarkably similar to the results for 0–200 cm. The trend of simulated soil moisture matches well with the result of GLDAS soil moisture, which shows a marked drying trend in the transitional regions between dry and wet

climates with a drying peak in the AI range of 0.4 to 0.8. In the same manner as the result of the soil moisture predictand shown in Figure 8, the trend of ConPrep soil moisture in the transitional regions was slightly smaller than the soil moisture trend. Also, the trend of ConTemp soil moisture was positive over most regions. This indicates that temperature was the key factor that caused the enhanced soil moisture drying in the transitional regions, which is in accordance with the results illustrated by the soil moisture predictand.

4. Summary and Discussion

Soil moisture is a key element in land surface processes, and it plays a vital role in water and energy cycles. This study used the GLDAS data to investigate the soil moisture variability for the period from 1948 to 2010. Soil moisture exhibited a long-term decreasing trend during the last several decades. However, the trend of soil moisture was spatially heterogeneous, with the most prominent wetting trend occurring over the central U.S., South America, and western Australia and drying over northern Africa, East Asia, eastern Australia, and southern Europe. The drying over the NAF and EAS regions was the most severe among the nine subregions detected by the relative drying acreage and contributions to global drying. The regionally averaged soil moisture trend as a function of the climatological mean AI showed that the most remarkable drying occurred over transitional regions between dry and wet areas, within the AI range of 0.4 to 0.8. In addition, the percent areas of drying over transitional regions were also the most obvious, with more than 60% of areas exhibiting negative soil moisture trends. The evolution of soil moisture trends detected by MEEMD showed that soil moisture drying was only significant over the transitional regions, but with a two-band structure. Noticeable drying first took place in the humid transitional regions within the AI range of 0.65 to 0.9 around 1955 and reached extremes around the 1990s. Along with the growing amplitude of the drying, the scope of drying expanded toward the dry transitional region (within the AI range of 0.4 to 0.65), beginning in the 1980s.

Linear regression analysis showed that the long-term trend of soil moisture is notably related to changes in precipitation and temperature. Nevertheless, the role of each differs individually. The precipitation change mainly affects the sign of soil moisture change: decreased precipitation causes drying, and increased precipitation causes wetting. In contrast, global warming has a negative effect on the soil moisture trend over most regions, even in wetting regions, and the effect on soil moisture drying is more apparent than that of precipitation. For the global average, precipitation has a dominant effect on the variability of soil moisture at interannual to decadal time scales, but temperature is the main cause of the long-term soil moisture trend on the whole. Thus, temperature is the key factor that caused the enhanced soil moisture drying in the transitional regions. We carried out three experiments based on the Noah-MP land surface model to verify the results obtained using linear regression methods, which accorded with the results illustrated by the soil moisture predictand.

In fact, drying and drought and analysis of their underlying mechanisms have been the subject of much recent research, especially over the African Sahel and East Asia, where the most severe drying occurred [*Rodríguez Fonseca et al*., 2015; *Zhang and Zhou*, 2015]. Drought in the African Sahel has often been explained as a combined effect of large-scale anomalies in sea surface temperature (SST) and positive vegetation-atmosphere feedbacks in recent studies. Previous studies have shown that warming of the equatorial Atlantic and Pacific/Indian Oceans at interannual time scales [*Biasutti et al*., 2008; *Mohino et al*., 2011a, 2011b] and warming over the tropics at decadal time scales [*Caminade and Terray*, 2010; *Hagos and Cook*, 2008] can result in rainfall reduction and drought over the Sahel. The local vegetation-atmosphere interactions were also important contributors to the Africa Sahel drought resulting from the remote effects of SST anomalies [*Kucharski et al*., 2013; *Wang et al*., 2004], because Africa has the largest influence of vegetation-atmosphere interactions in the world [*Xue et al*., 2010]. East Asia is also greatly impacted by drying and drought. Most of East Asia is dominated by monsoonal circulation, and the summer monsoon rainfall accounts for much of the annual precipitation [*Wang et al*., 2012]. Thus, the drying trend over East Asia is a regional manifestation of a long-term or interdecadal change in precipitation associated with the interdecadal weakening of the East Asian summer monsoon circulation, which is driven by the phase transition of the Pacific Decadal Oscillation [*Zhang and Zhou*, 2015]. In addition, temperature warming is also a key factor to the East Asia drying. Studies show that temperature warming enhances soil drying almost twofold, driven by decreasing precipitation over East Asia [*Cheng et al*., 2015].

As mentioned above, temperature can affect soil moisture through changing soil evapotranspiration. With decreasing soil moisture, the evapotranspiration may thus be reduced, possibly leading to an increase in

the sensible heat flux and a further temperature increase [*Huang et al*., 2015b]. The increased temperature, decreased evapotranspiration, and soil moisture form a positive feedback, and this positive feedback can continue until the soil is totally dry and desertification results, if the feedback loop is not broken. This would destroy the ecological environment, depress crop production, and cause dust [*Huang et al*., 2006, 2009; *Kim and Choi*, 2015] and drought [*Huang et al*., 2015b]. This effect is most serious in the transitional regions because the surface climate is the most sensitive to soil moisture in transitional climate regions that are neither very dry nor very wet [*Koster et al*., 2004; *Seneviratne et al*., 2010]. In a transitional climate region, soil moisture is the main factor controlling the partitioning of total surface energy in sensible and latent heat fluxes and consequently also on the near-surface temperature and evapotranspiration. Also, increasing temperature and drying are the most severe in transitional climate regions. The strongest positive feedback between severe warming and drying could further enhance the drying trend and make the dry land even drier. Additionally, transitional regions are normally agricultural districts with large populations. Their ecosystems tend to be fragile and sensitive to the climate change; a slight disturbance in climate is likely to cause devastating consequences. The most serious warming and drying would pose a great challenge to the ecosystem as well as human survival. Strict management and rational schemes to use water resources, therefore, are in urgent need so as to alleviate the enormous impact of the drying.

Acknowledgments

We thank the NASA/GSFC and NOAA/NCEP for producing and making available the GLDAS data sets. The GLDAS data sets are available via the Mirador data archive search interface (http://mirador.gsfc.nasa.gov/). Data set names: GLDAS_NOAH10_M_020 (Analysis data) and GLDAS_NOAH10_3H_020 (Forcing data of Noah-MP). All of the authors thank Song Feng for providing the AI data sets and Zongliang Yang for providing the static data sets of the Noah-MP. This work was jointly supported by the National Science Foundation of China (41521004 and 41305009), the National Basic Research Program of China (2012CB955301), and the China 111 project (B13045).

References

Biasutti, M., I. Held, A. Sobel, and A. Giannini (2008), SST forcings and Sahel rainfall variability in simulations of the twentieth and twenty-first centuries, *J. Clim.*, *21*(14), 3471–3486, doi:10.1175/2007JCLI1896.1.

Brocca, L., et al. (2011), Soil moisture estimation through ASCAT and AMSR-E sensors: An intercomparison and validation study across Europe, *Remote Sens. Environ.*, *115*(12), 3390–3408, doi:10.1016/j.rse.2011.08.003.

Brocca, L., T. Tullo, F. Melone, T. Moramarco, and R. Morbidelli (2012), Catchment scale soil moisture spatial–temporal variability, *J. Hydrol.*, *422*, 63–75, doi:10.1016/j.jhydrol.2011.12.039.

Caminade, C., and L. Terray (2010), Twentieth century Sahel rainfall variability as simulated by the ARPEGE AGCM, and future changes, *Clim. Dyn.*, *35*(1), 75–94, doi:10.1007/s00382-009-0545-4.

Chandler, R., and M. Scott (2011), *Statistical Methods for Trend Detection and Analysis in the Environmental Sciences*, John Wiley, Chichester, U. K., doi:10.1002/9781119991571.

Chen, F., and J. Dudhia (2001), Coupling an advanced land surface-hydrology model with the Penn State-NCAR MM5 modeling system. Part I: Model implementation and sensitivity, *Mon. Weather Rev.*, *129*(4), 569–585, doi:10.1175/1520-0493(2001)129<0569:CAALSH>2.0.CO;2.

Chen, F., K. Mitchell, J. Schaake, Y. Xue, H. L. Pan, V. Koren, Q. Y. Duan, M. Ek, and A. Betts (1996), Modeling of land surface evaporation by four schemes and comparison with FIFE observations, *J. Geophys. Res.*, *101*, 7251–7268, doi:10.1029/95JD02165.

Chen, F., Z. Janjić, and K. Mitchell (1997), Impact of atmospheric surface-layer parameterizations in the new land-surface scheme of the NCEP mesoscale Eta model, *Boundary Layer Meteorol.*, *85*(3), 391–421, doi:10.1023/A:1000531001463.

Cheng, S., X. Guan, J. Huang, F. Ji, and R. Guo (2015), Long-term trend and variability of soil moisture over East Asia, *J. Geophys. Res. Atmos.*, *120*, 8658–8670, doi:10.1002/2015JD023206.

Ciais, P., et al. (2005), Europe-wide reduction in primary productivity caused by the heat and drought in 2003, *Nature*, *437*(7058), 529–533, doi:10.1038/nature03972.

Cook, B. I., G. B. Bonan, and S. Levis (2006), Soil moisture feedbacks to precipitation in southern Africa, *J. Clim.*, *19*(17), 4198–4206, doi:10.1175/JCLI3856.1.

Dai, A. (2011), Drought under global warming: A review, *WIRES Clim. Change*, *2*(1), 45–65, doi:10.1002/wcc.81.

Dai, A. (2013), Increasing drought under global warming in observations and models, *Nat. Clim. Change*, *3*(1), 52–58, doi:10.1038/nclimate1633.

Dai, A., K. E. Trenberth, and T. Qian (2004), A global dataset of Palmer Drought Severity Index for 1870–2002: Relationship with soil moisture and effects of surface warming, *J. Hydrometeorol.*, *5*(6), 1117–1130, doi:10.1175/JHM-386.1.

Dorigo, W., R. Jeu, D. Chung, R. Parinussa, Y. Liu, W. Wagner, and D. Fernández-Prieto (2012), Evaluating global trends (1988–2010) in harmonized multi-satellite surface soil moisture, *Geophys. Res. Lett.*, *39*, L18405, doi:10.1029/2012GL052988.

Feng, S., and Q. Fu (2013), Expansion of global drylands under a warming climate, *Atmos. Chem. Phys.*, *13*(19), 10,081–10,094, doi:10.5194/acp-13-10081-2013.

Findell, K. L., and E. A. Eltahir (2003a), Atmospheric controls on soil moisture-boundary layer interactions. Part I: Framework development, *J. Hydrometeorol.*, *4*(3), 552–569, doi:10.1175/1525-7541(2003)004<0552:ACOSML>2.0.CO;2.

Findell, K. L., and E. A. Eltahir (2003b), Atmospheric controls on soil moisture-boundary layer interactions. Part II: Feedbacks within the continental United States, *J. Hydrometeorol.*, *4*(3), 570–583, doi:10.1175/1525-7541(2003)004<0570:ACOSML>2.0.CO;2.

Guan, X., J. Huang, N. Guo, J. Bi, and G. Wang (2009), Variability of soil moisture and its relationship with surface albedo and soil thermal parameters over the Loess Plateau, *Adv. Atmos. Sci.*, *26*(4), 692–700, doi:10.1007/s00376-009-8198-0.

Hagos, S. M., and K. H. Cook (2008), Ocean warming and late-twentieth-century Sahel drought and recovery, *J. Clim.*, *21*(15), 3797–3814, doi:10.1175/2008JCLI2055.1.

Hirschi, M., S. I. Seneviratne, V. Alexandrov, F. Boberg, C. Boroneant, O. B. Christensen, H. Formayer, B. Orlowsky, and P. Stepanek (2011), Observational evidence for soil-moisture impact on hot extremes in southeastern Europe, *Nat. Geosci.*, *4*(1), 17–21, doi:10.1038/NGEO1032.

Huang, J., B. Lin, P. Minnis, T. Wang, X. Wang, Y. Hu, Y. Yi, and J. K. Ayers (2006), Satellite-based assessment of possible dust aerosols semi-direct effect on cloud water path over East Asia, *Geophys. Res. Lett.*, *33*, L19802, doi:10.1029/2006GL026561.

Huang, J., et al. (2008), An overview of the semi-arid climate and environment research observatory over the Loess Plateau, *Adv. Atmos. Sci.*, *25*(6), 906–921, doi:10.1007/s00376-008-0906-7.

Huang, J., Q. Fu, J. Su, Q. Tang, P. Minnis, Y. Hu, Y. Yi, and Q. Zhao (2009), Taklimakan dust aerosol radiative heating derived from CALIPSO observations using the Fu-Liou radiation model with CERES constraints, *Atmos. Chem. Phys.*, *9*(12), 4011–4021, doi:10.5194/acp-9-4011-2009.

Huang, J., X. Guan, and F. Ji (2012), Enhanced cold-season warming in semi-arid regions, *Atmos. Chem. Phys.*, *12*(12), 5391–5398, doi:10.5194/acp-12-5391-2012.
Huang, J., M. Ji, Y. Xie, S. Wang, Y. He, and J. Ran (2015a), Global semi-arid climate change over last 60 years, *Clim. Dyn.*, *46*, 1131–1150, doi:10.1007/s00382-015-2636-8.
Huang, J., H. Yu, X. Guan, G. Wang, and R. Guo (2015b), Accelerated dryland expansion under climate change, *Nat. Clim. Change*, doi:10.1038/nclimate2837.
Huang, N. E., Z. Shen, S. R. Long, M. C. Wu, H. H. Shih, Q. Zheng, N. Yen, C. C. Tung, and H. H. Liu (1998), The empirical mode decomposition and the Hilbert spectrum for nonlinear and non-stationary time series analysis, *Proc. R. Soc. London*, *454*, 903–995.
Ji, F., Z. Wu, J. Huang, and E. P. Chassignet (2014), Evolution of land surface air temperature trend, *Nat. Clim. Change*, *4*(6), 462–466, doi:10.1038/nclimate2223.
Kim, H., and M. Choi (2015), Impact of soil moisture on dust outbreaks in East Asia: Using satellite and assimilation data, *Geophys. Res. Lett.*, *42*, 2789–2796, doi:10.1002/2015GL063325.
Koster, R. D., et al. (2004), Regions of strong coupling between soil moisture and precipitation, *Science*, *305*(5687), 1138–1140, doi:10.1126/science.1100217.
Kucharski, F., N. Zeng, and E. Kalnay (2013), A further assessment of vegetation feedback on decadal Sahel rainfall variability, *Clim. Dyn.*, *40*(5), 1453–1466, doi:10.1007/s00382-012-1397-x.
Lawrence, J. E., and G. M. Hornberger (2007), Soil moisture variability across climate zones, *Geophys. Res. Lett.*, *34*, L20402, doi:10.1029/2007GL031382.
Li, Y., J. Huang, M. Ji, and J. Ran (2014), Dryland expansion in northern China from 1948 to 2008, *Adv. Atmos. Sci.*, *32*(6), 870–876, doi:10.1007/s00376-014-4106-3.
Lin, B., P. W. Stackhouse, P. Minnis, B. A. Wielicki, Y. Hu, W. Sun, T. F. Fan, and L. M. Hinkelman (2008), Assessment of global annual atmospheric energy balance from satellite observations, *J. Geophys. Res.*, *113*, D16114, doi:10.1029/2008JD009869.
Lorenz, R., E. Davin, and S. Seneviratne (2012), Modeling land-climate coupling in Europe: Impact of land surface representation on climate variability and extremes, *J. Geophys. Res.*, *117*, D20109, doi:10.1029/2012JD017755.
Middleton, N., and D. Thomas (1997), *World Atlas of Desertification*, Arnold, London.
Mohino, E., B. Rodríguez-Fonseca, T. Losada, S. Gervois, S. Janicot, J. Bader, P. Ruti, and F. Chauvin (2011a), Changes in the interannual SST-forced signals on West African rainfall. AGCM intercomparison, *Clim. Dyn.*, *37*(9), 1707–1725, doi:10.1007/s00382-011-1093-2.
Mohino, E., B. Rodríguez-Fonseca, C. Mechoso, S. Gervois, P. Ruti, and F. Chauvin (2011b), Impacts of the tropical Pacific/Indian Oceans on the seasonal cycle of the West African monsoon, *J. Clim.*, *24*(15), 3878–3891, doi:10.1175/2011JCLI3988.1.
Niu, G., et al. (2011), The community Noah land surface model with multiparameterization options (Noah-MP): 1. Model description and evaluation with local-scale measurements, *J. Geophys. Res.*, *116*, D12109, doi:10.1029/2010JD015139.
Polyakov, I. V., V. A. Alexeev, U. S. Bhatt, E. I. Polyakova, and X. Zhang (2010), North Atlantic warming: Patterns of long-term trend and multidecadal variability, *Clim. Dyn.*, *34*(2), 439–457, doi:10.1007/s00382-008-0522-3.
Reichle, R. H., R. D. Koster, P. Liu, S. P. Mahanama, E. G. Njoku, and M. Owe (2007), Comparison and assimilation of global soil moisture retrievals from the Advanced Microwave Scanning Radiometer for the Earth Observing System (AMSR-E) and the Scanning Multichannel Microwave Radiometer (SMMR), *J. Geophys. Res.*, *112*, D09108, doi:10.1029/2006JD008033.
Reichstein, M., et al. (2007), Reduction of ecosystem productivity and respiration during the European summer 2003 climate anomaly: A joint flux tower, remote sensing and modelling analysis, *Global Change Biol.*, *13*(3), 634–651, doi:10.1111/j.1365-2486.2006.01224.x.
Rodell, M., et al. (2004), The global land data assimilation system, *Bull. Am. Meteorol. Soc.*, *85*(3), 381–394, doi:10.1175/BAMS-85-3-381.
Rodríguez Fonseca, B., et al. (2015), Variability and predictability of West African droughts: A review on the role of sea surface temperature anomalies, *J. Clim.*, *28*(10), 4034–4060, doi:10.1175/JCLI-D-14-00130.1.
Seneviratne, S. I., T. Corti, E. L. Davin, M. Hirschi, E. B. Jaeger, I. Lehner, B. Orlowsky, and A. J. Teuling (2010), Investigating soil moisture–climate interactions in a changing climate: A review, *Earth Sci. Rev.*, *99*(3), 125–161, doi:10.1016/j.earscirev.2010.02.004.
Sheffield, J., and E. F. Wood (2008), Global trends and variability in soil moisture and drought characteristics, 1950–2000, from observation-driven simulations of the terrestrial hydrologic cycle, *J. Clim.*, *21*(3), 432–458, doi:10.1175/2007JCLI1822.1.
Sheffield, J., G. Goteti, and E. F. Wood (2006), Development of a 50-year high-resolution global dataset of meteorological forcings for land surface modeling, *J. Clim.*, *19*(13), 3088–3111, doi:10.1175/JCLI3790.1.
Ting, M., Y. Kushnir, R. Seager, and C. Li (2009), Forced and internal twentieth-century SST trends in the North Atlantic, *J. Clim.*, *22*(6), 1469–1481, doi:10.1175/2008JCLI2561.1.
Wang, B., J. Liu, H. Kim, P. J. Webster, and S. Yim (2012), Recent change of the global monsoon precipitation (1979–2008), *Clim. Dyn.*, *39*(5), 1123–1135, doi:10.1007/s00382-011-1266-z.
Wang, G., E. A. B. Eltahir, J. A. Foley, D. Pollard, and S. Levis (2004), Decadal variability of rainfall in the Sahel: Results from the coupled GENESIS-IBIS atmosphere-biosphere model, *Clim. Dyn.*, *22*(6), 625–637, doi:10.1007/s00382-004-0411-3.
Wang, G., J. Huang, W. Guo, J. Zuo, J. Wang, J. Bi, Z. Huang, and J. Shi (2010), Observation analysis of land-atmosphere interactions over the Loess Plateau of northwest China, *J. Geophys. Res.*, *115*, D00K17, doi:10.1029/2009JD013372.
Wang, H., J. C. Rogers, and D. K. Munroe (2015), Commonly used drought indices as indicators of soil moisture in China, *J. Hydrometeorol.*, *16*(3), 1397–1408, doi:10.1175/JHM-D-14-0076.1.
Wang, S., J. Huang, Y. He, and Y. Guan (2014), Combined effects of the Pacific Decadal Oscillation and El Niño-Southern Oscillation on global land dry–wet changes, *Sci. Rep.*, *4*, 6651, doi:10.1038/srep06651.
Wu, Z., N. E. Huang, and X. Chen (2009), The multi-dimensional ensemble empirical mode decomposition method, *Adv. Adapt. Data Anal.*, *1*(03), 339–372, doi:10.1142/S1793536909000187.
Wu, Z., N. E. Huang, J. M. Wallace, B. V. Smoliak, and X. Chen (2011), On the time-varying trend in global-mean surface temperature, *Clim. Dyn.*, *37*(3), 759–773, doi:10.1007/s00382-011-1128-8.
Xue, Y., F. De Sales, R. Vasic, C. R. Mechoso, A. Arakawa, and S. Prince (2010), Global and seasonal assessment of interactions between climate and vegetation biophysical processes: A GCM study with different land-vegetation representations, *J. Clim.*, *23*(6), 1411–1433, doi:10.1175/2009JCLI3054.1.
Yang, K., T. Watanabe, T. Koike, X. Li, H. Fujii, K. Tamagawa, Y. Ma, and H. Ishikawa (2007), Auto-calibration system developed to assimilate AMSR-E data into a land surface model for estimating soil moisture and the surface energy budget, *J. Meteorol. Soc. Jpn.*, *85A*, 229–242, doi:10.2151/jmsj.85A.229.
Yang, K., T. Koike, I. Kaihotsu, and J. Qin (2009), Validation of a dual-pass microwave land data assimilation system for estimating surface soil moisture in semiarid regions, *J. Hydrometeorol.*, *10*(3), 780–793, doi:10.1175/2008JHM1065.1.
Yang, Z., et al. (2011), The community Noah land surface model with multiparameterization options (Noah-MP): 2. Evaluation over global river basins, *J. Geophys. Res.*, *116*, D12110, doi:10.1029/2010JD015140.
Zhang, L., and T. Zhou (2015), Drought over East Asia: A review, *J. Clim.*, *28*(8), 3375–3399, doi:10.1175/JCLI-D-14-00259.1.